Wave Inversion Technology, Report No. 4, pages 7-19

New features of the Common-Reflection-Surface Stack

Jürgen Mann and Alex Gerst[1]

keywords: *conflicting dips, multiple attenuation, wavefield attributes*

ABSTRACT

The Common-Refection-Surface (CRS) stack is macro-model independent seismic reflection imaging method that provides a simulated zero-offset (ZO) section as well as kinematic wavefield attributes from 2-D multi-coverage data. The underlying theory, the implementation strategy, and applications of the method were thoroughly discussed in the preceeding annual reports. However, the pragmatic search strategy described in these reports assigns only one optimum stacking operator to each ZO sample to be simulated. Consequently, in case of intersecting events, this approach only images and characterizes the most prominent event instead of all contributing events. To overcome this limitation, we introduce an extended CRS stack method that allows to consider conflicting dip situations. Combined with an improved handling of stacking velocity constraints, the extended method is better suited to attenuate multiples and to reveal and characterize primary events formerly obscured by multiples. Each event contributing to a particular ZO sample is now separately stacked and described by means of its associated wavefield attributes. Thus, the interference of intersecting events can be simulated to obtain a more realistic ZO section as input for subsequent post-stack processing. Furthermore, the wavefield attributes associated with an event are now more contiguous along the event, even if the event interferes with an intersecting event. This provides a more complete and reliable basis for a multitude of applications of the wavefield attributes like, e. g., an approximate time migration or a layer-based inversion of the depth model. We present and discuss some of the first results obtained with the extended CRS stack strategy.

INTRODUCTION

The CRS stack method (Müller, 1998, 1999) simulates a ZO section by summing along stacking surfaces in the multi-coverage data. The stacking operator is an approximation of the kinematic reflection response of a curved interface in a laterally inhomogeneous medium. Three kinematic attributes associated with wavefronts of

[1]**email:** Juergen.Mann@gpi.uni-karlsruhe.de

two hypothetical eigenwave experiments are the parameters of the stacking operator. Coherency analyses along various test stacking operators are performed for each particular ZO sample to be simulated. The stacking operator (and its three associated wavefield attributes) yielding the highest coherency is used to perform the actual stack.

Unfortunately, not only one event might contribute to a particular ZO sample, but different events may intersect at the considered ZO location. In case of bow-tie structures, an event will even intersect itself. To properly simulate a ZO section under such conditions, it is no longer sufficient to consider only one stacking operator for each ZO sample, but we have to determine separate stacking operators for each contributing event (or segment of a bow-tie structure). The final stack result can be constructed as a superposition of the contributions of all separate stacking operators.

Figure 1a shows a detail of a simulated ZO section with a bow-tie structure as obtained by the CRS stack without consideration of conflicting dips. The interference of the bow-tie segments is incorrectly simulated. The less prominent bow-tie segment is suppressed at the intersection point and thus broken into two parts.

The modeled ZO section of the synthetic data set used for this example is shown in Figure 1b. As expected, the bow-tie segments interfere and the section differs significantly from the ZO section simulated by means of the CRS stack (Figure 1a). An ideal CRS stack algorithm should yield the ZO section of Figure 1b rather than that of Figure 1a.

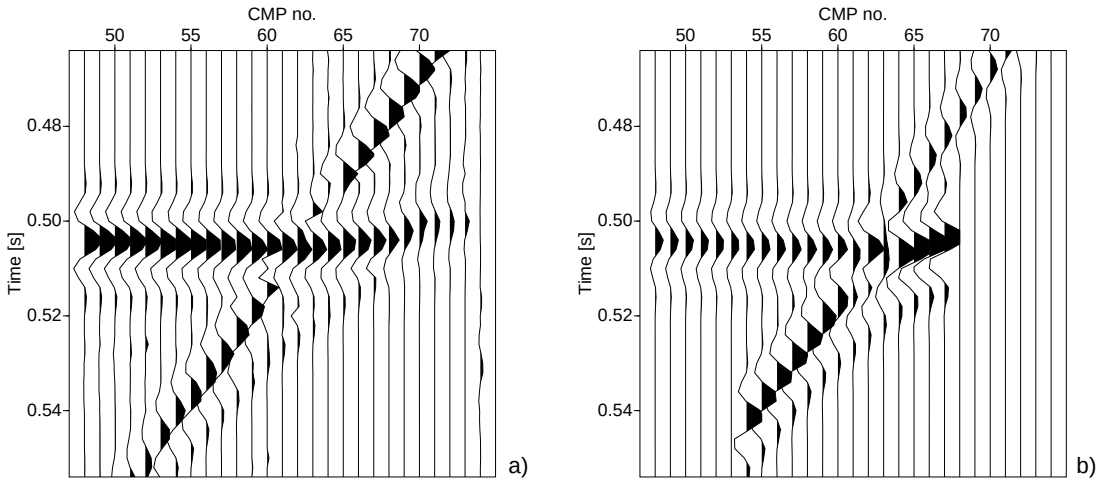

Figure 1: a) Detail of a simulated ZO section for a synthetic data set. Conflicting dips are not considered in this application of the CRS stack, therefore the steeper bow-tie segment is broken instead of interfering with the flat bow-tie segment. b) Detail of the modeled ZO section of the synthetic data set used as input for the result shown in subfigure a). The interference of the intersecting bow-tie segments is clearly visible.

The lack of coherent energy along the steeper bow-tie segment will cause a shadow zone in a subsequent post-stack migration. Furthermore, no wavefield attributes for this segment are available in the region of intersection. Such gaps in the wavefield attribute sections will cause difficulties in subsequent applications of the attributes. This is illustrated in Figure 2 for a real data set: this figure shows a detail of a wavefield attribute based approximate time migration (Mann et al., 2000) without (Figure 2a) and with (Figure 2b) considering conflicting dips. In the former case, some reflection events are broken due to the missing wavefield attributes.

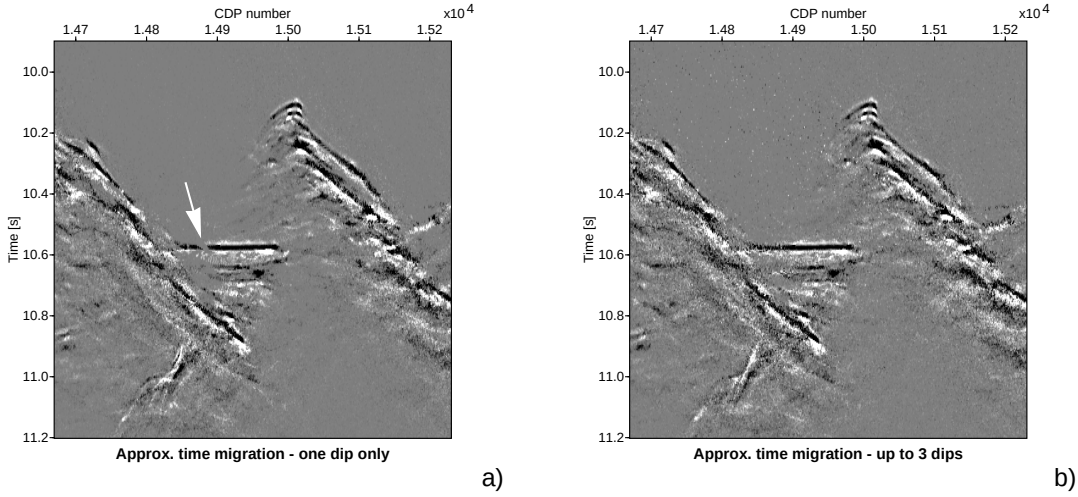

Figure 2: Details of a wavefield attribute based approximate time migration generated a) with the most prominent event only, b) with up to three conflicting dips. The arrow indicates a reflector segment that is broken in the former case.

PRAGMATIC SEARCH STRATEGY

To be able to follow the pragmatic approach of (Müller, 1998), let us briefly review some theoretical aspects of the CRS stack: we use a hyperbolic second order representation of the CRS stacking operator which can be derived by means of paraxial ray theory (Schleicher et al., 1993; Tygel et al., 1997). Three independent parameters are used to account for the local properties of the subsurface interfaces: the angle of emergence α of the normal ray and the two radii of curvature R_N and R_{NIP} associated with two hypothetical eigenwave experiments (see e. g. (Mann et al., 1999)). The stacking operator reads

$$\begin{aligned} t^2\left(x_m, h\right) &= \left(t_0 + \frac{2\,\sin\,\alpha}{v_0}\left(x_m - x_0\right)\right)^2 \\ &+ \frac{2\,t_0\,\cos^2\,\alpha}{v_0}\left(\frac{\left(x_m - x_0\right)^2}{R_N} + \frac{h^2}{R_{NIP}}\right)\,, \end{aligned} \tag{1}$$

where the half-offset between source and receiver is denoted by h, and x_m denotes the midpoint between source and receiver. The only required model parameter is the near surface velocity v_0. The respective sample of the ZO trace to be simulated is defined by (t_0, x_0).

The CRS stack consists of a measure of the coherency of the multi-coverage data along all operators given by Equation (1) for any possible combination of values of α, R_{NIP}, and R_N within a specified test range.

In principle, we have to determine the global maximum and a set of local maxima of the coherency measure in the three-parametric attribute domain. However, even the determination of the global maximum turns out to be too time consuming in a three-parametric search strategy. Therefore, we cannot expect to be able to detect additional local maxima in this way.

(Müller, 1998) proposed to split the three-parametric problem into three one-parametric searches and an optional three-parametric local optimization as depicted in the following simplified flowchart:

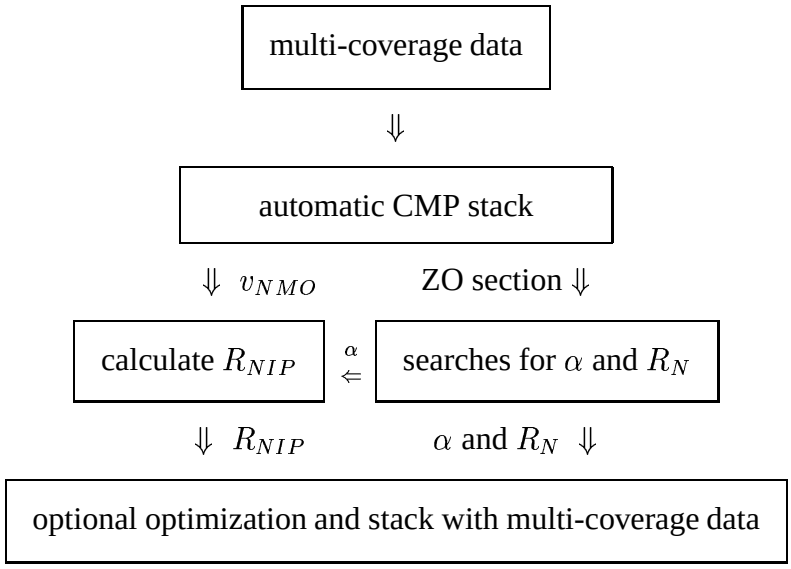

The first search step of this pragmatic approach is an automatic CMP stack. The search parameter is the stacking velocity v_{NMO} which can be written in terms of the CRS wavefield attributes as

$$v_{NMO}^2 = \frac{2\, v_0\, R_{NIP}}{t_0\, \cos^2 \alpha}\ . \tag{2}$$

The next two search steps are applied to the CMP stacked section. The search parameters are α and R_N. The former is then used to calculate R_{NIP} by means of formula (2).

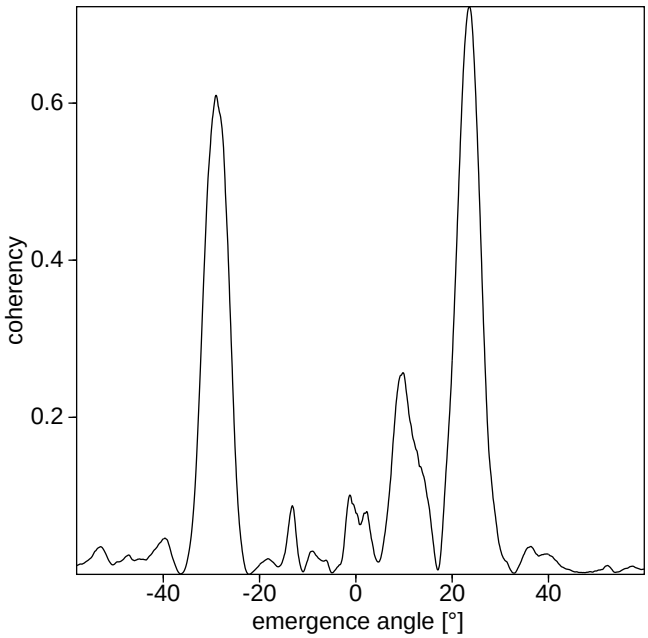

Figure 3: Coherency measure plotted versus the tested angles of emergence of the normal ray. Distinct local maxima can be observed, although conflicting dips have not been considered in the preceeding step.

CONFLICTING DIPS

This three-step strategy has to be modified if conflicting dips are to be correctly taken into account. Unfortunately, in spite of the angle-dependence of v_{NMO}, we cannot rely on the first step to separate events with different emergence angles because the associated stacking velocities might be similar or even identical. Furthermore, the sign of the emergence angle α cannot be determined by means of Equation (2).

However, it is possible to detect events with different emergence angles in the second step in the CMP stacked section, although these have not been correctly taken into account by the preceeding automatic CMP stack. This is indicated by Figure 3, which was obtained from a real data example. For a given point in the ZO section to be simulated the coherency values are plotted versus the tested emergence angles. We observe three distinct local maxima which are potential candidates for conflicting dips.

We have computed the "angle spectrum" depicted in Figure 3 for a deep-offshore data set. At the considered ZO location, two diffraction patterns (at $\alpha \approx -30^\circ$ and $\alpha \approx 25^\circ$, respectively) and a weak reflection event (at $\alpha \approx 12^\circ$) intersect each other.

Due to the above observations, the three-step approach can be easily extended such as to detect conflicting events with different emergence angles. However, the calculation of R_{NIP} from α and v_{NMO} according to Equation (2) is no longer possible, because, in general, we will detect more than one angle of emergence but only one value for the stacking velocity v_{NMO}. Consequently, the approach has to be adapted to account for this fact. An additional search procedure for each radius of curvature

$R_{NIP}^{(i)}$ corresponding to each conflicting dip $\alpha^{(i)}$ becomes necessary.

Unfortunately, $R_{NIP}^{(i)}$ can be determined neither in the CMP stacked section nor in the original CMP gathers. According to the stacking operator (1), $R_{NIP}^{(i)}$ has no influence in the ZO section $(h = 0)$, and in the CMP gather $(x_m = x_0)$, $R_{NIP}^{(i)}$ and $\alpha^{(i)}$ cannot be separated. To solve this problem, we propose to perform the additional search for $R_{NIP}^{(i)}$ in another subset of the multi-coverage data, namely in the common-shot/common-receiver (CS/CR) gather. This gather is defined by the condition $|x_m - x0| \approx |h|$. A simplified flowchart of this strategy is depicted in the following flowchart:

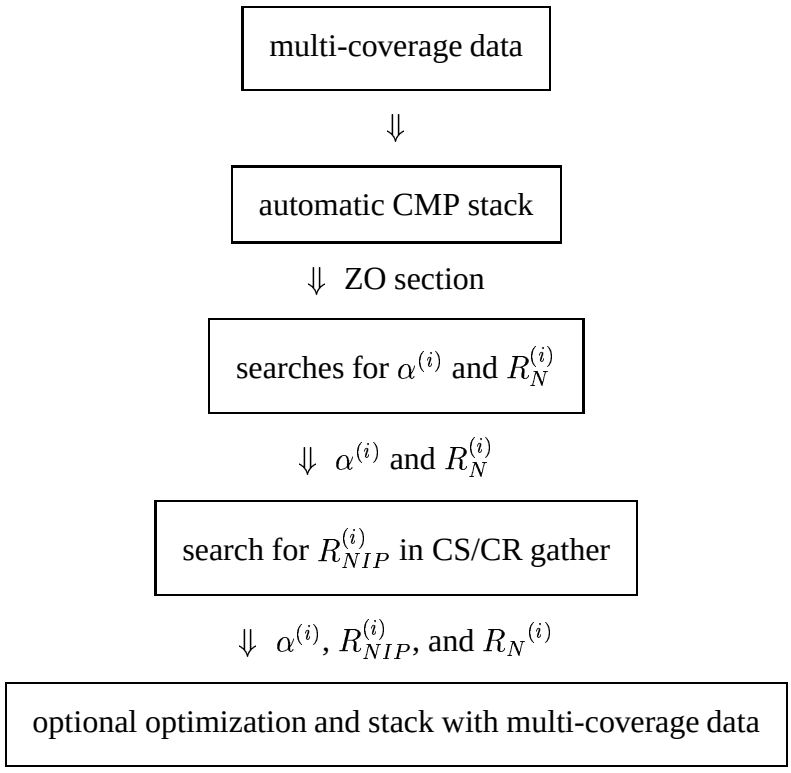

The index i denotes the different events detected for one and the same ZO sample. If only one event for a particular ZO sample is detected, we can still use the pragmatic scheme without the explicit search for $R_{NIP}^{(i)}$. Otherwise, the automatic CMP stack only serves to provide a simulated ZO section in which $\alpha^{(i)}$ and $R_N^{(i)}$ can be easily detected, whereas the stacking velocity is not explicitly used anymore.

The additional one-parametric search for $R_{NIP}^{(i)}$ is almost identical as the already implemented search for $R_N^{(i)}$. Thus, a new algorithm to perform this search is not required.

The determination of the emergence angles is based on an approximation of the CRS operator (1) for $R_N = \pm\infty$ in the ZO section $(x_m = x_0)$. This implies that

we are looking for plane waves emerging at the surface. This assumption only holds in a relatively small aperture around the emergence location of the normal ray. As a consequence, the number of contributing traces is small and the algorithm usually tends to detect emergence angles which are related to artifacts in the data rather than to actual events, too. Such cases can be easily identified and eliminated in the subsequent search for R_N, because this search will yield very low coherency values for "wrong" emergence angles associated with small plane artifacts.

STACKING VELOCITY CONSTRAINTS

The first step of the CRS stack approach, the automatic CMP stack, is very similar to the conventional CMP stack method. Consequently, multiples with moveouts different from the moveouts of neighboring primary events can be attenuated in the CRS stack by applying stacking velocity constraints.

For the CRS stack, this approach was already introduced and applied by (Müller, 1999). However, it is not sufficient to simply restrict the range of tested stacking velocities and to select the stacking velocity yielding the highest coherence value. The stacking velocity detected in this way might be located at the margin of the tested range. In general, such a value does not correspond to an actual maximum in the velocity spectrum and yields misleading results.

We improved the handling of stacking velocity constraints by adding an automatic analysis of the velocity spectrum. By means of this analysis, we determine the largest local maximum *inside* the tested velocity range. This leads to a smoother stacking velocity section and a better attenuation of the multiples.

Returning to the flowcharts of the CRS stack method, we observe that two of the wavefield attributes, α and R_N, are determined in the result of the automatic CMP stack which no longer provides any information about offset-dependent moveouts. Unfortunately, an attenuated multiple in the CMP stack result might still be the most prominent event (at least locally). Consequently, only the combination of stacking velocity constraints *and* conflicting dip handling enables us to detect, stack, and characterize potential primary events obscured by multiples.

From our point of view, this strategy is not intended for an efficient removal of multiples, but as an possibility to increase the probability to successfully detect obscured primary events. The multiples will still be contained in the results, but conflicting primary events will most likely be preferred.

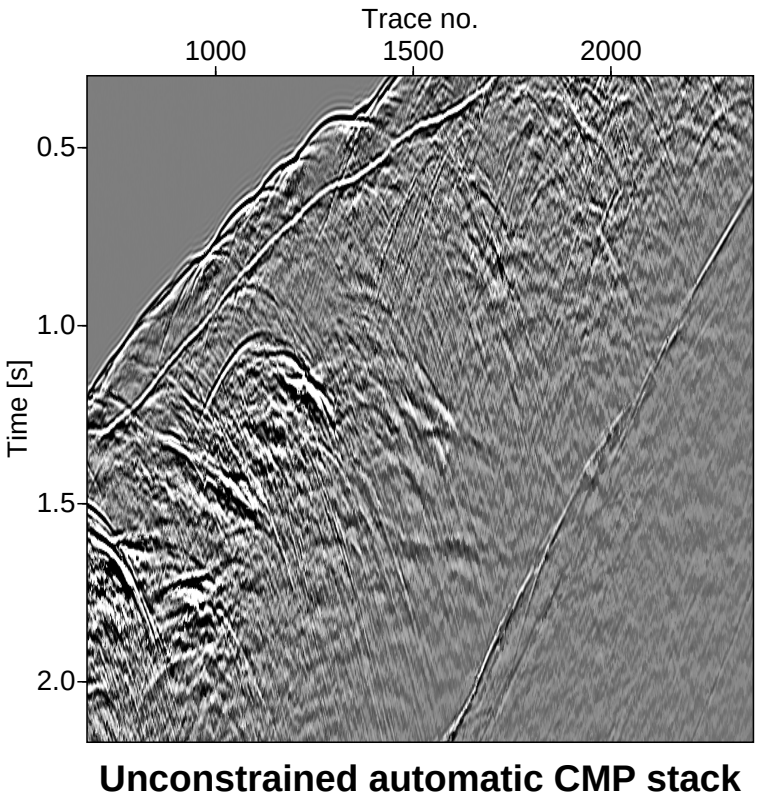

Figure 4: Result of the unconstrained automatic CMP stack. Multiples of the sea-floor and the BSR are clearly visible.

FIRST RESULTS

We applied the extended CRS stack strategy for the very first time to a marine data set acquired offshore Costa Rica. These data were acquired and provided by the Bundesanstalt für Geowissenschaften und Rohstoffe, Hannover, Germany. The complete results—a set of 62 output sections—go far beyond the scope of this paper. Therefore, we focus on some small subsets of the results to illustrate the effects of the newly introduced features.

The processed data have a sampling rate of 4 ms and a CDP bin distance of 6.25 m. The maximum fold in the CMP gathers is 49. As first processing step we applied an automatic CMP stack with very weak stacking velocity constraints. The result is shown in Figure 4. We observe strong multiples of the sea-floor as well as of the BSR beneath it. The multiples can also easily be identified in the corresponding stacking velocity section (not shown).

We picked a set of traveltimes slightly above the multiples to set up a very simple model of stacking velocity constraints in a way that water velocity is no longer

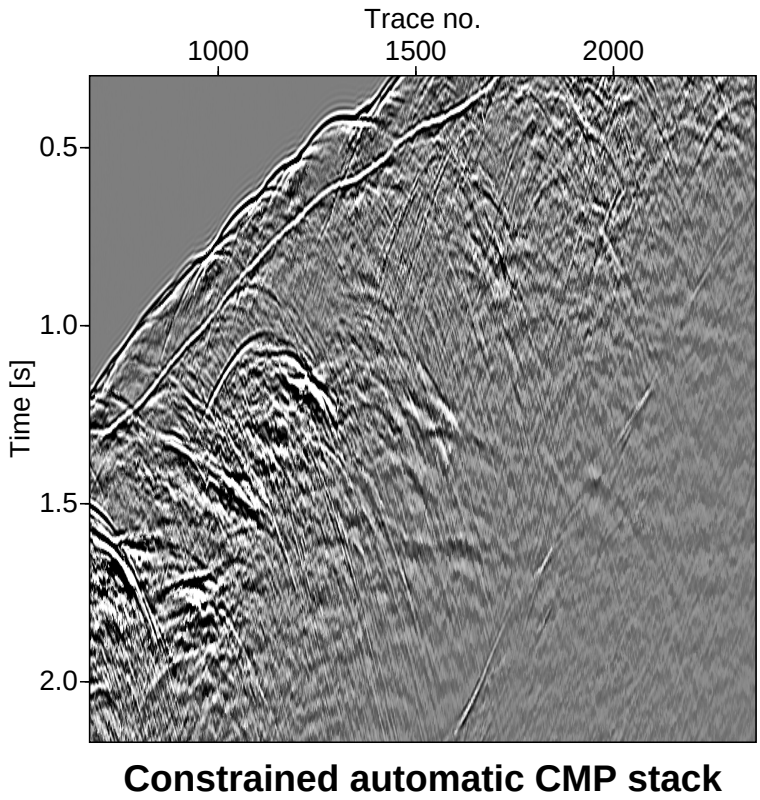

Figure 5: Result of the constrained automatic CMP stack. The multiples of the sea-floor and the BSR are significantly attenuated.

allowed in the vicinity of the multiples. As can be seen in Figure 5, the multiples are significantly attenuated in the now constrained automatic CMP stack. This increases the probability to detect primary events at these locations.

In the next processing step, our aim is to detect conflicting dip situations in the result of the constrained automatic CMP stack. For this task we have to automatically analyze coherence spectra of the kind shown in Figure 3. This requires the definition of a set of thresholds to detect a discrete number of contributing events. For this example, conflicting dips were accepted if the most prominent event reaches a semblance value of 0.6 and the local maxima reach 40% of the global maximum. As a by-product of this step, we receive a map with the number of detected conflicting events (not displayed).

To briefly illustrate the effect of the conflicting dip handling, details of the final stack result and the emergence angle sections are shown in Figure 6. At locations were only one event has been detected, the emergence angle for the second contributing event (Figure 6d) is replaced by the angle associated with the first (and, in this case, only) event. This preserves the spatial context of this attribute section, which otherwise would be only sparsely covered with values.

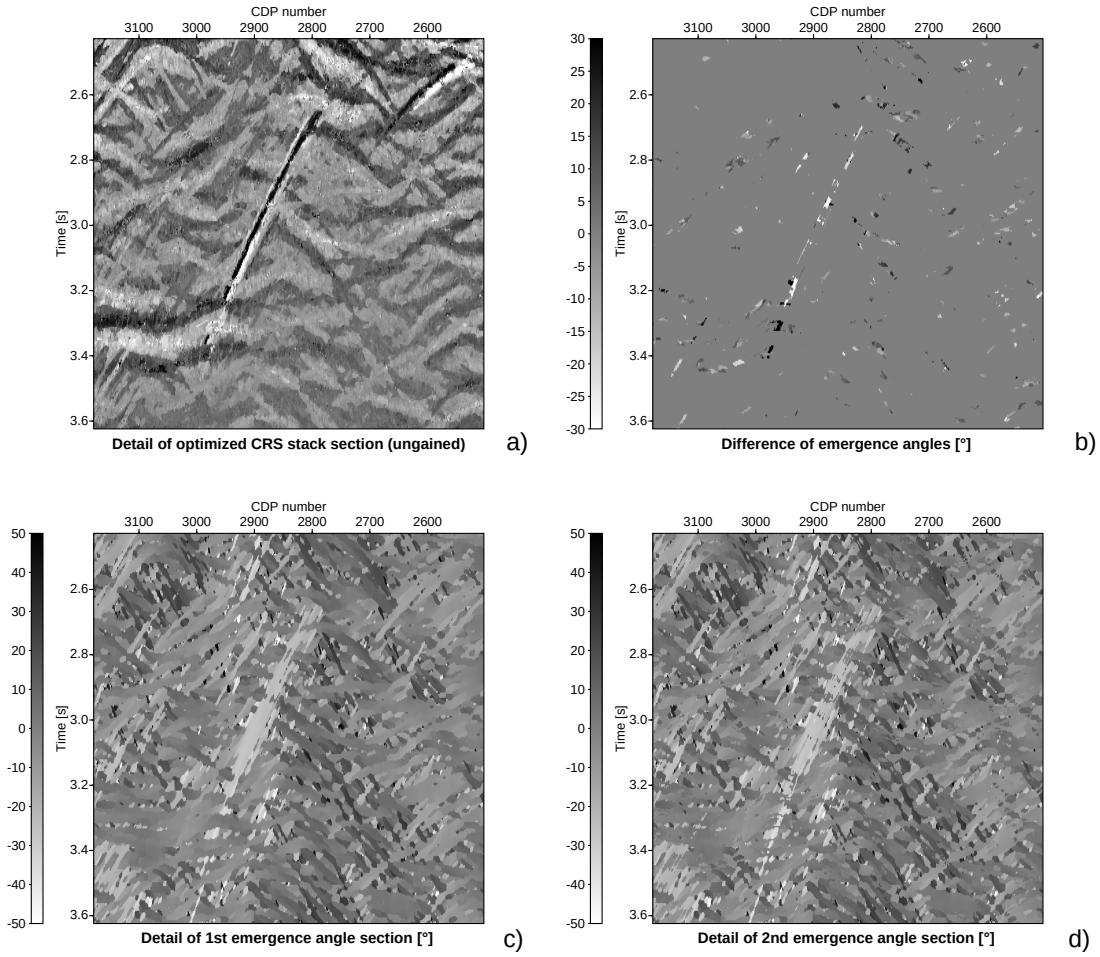

Figure 6: Details of the CRS stack results: a) optimized CRS stack section, c) and d) emergence angles of the first and second detected contributing events, b) difference of the emergence angles shown in c) and d).

The steep event in the center of the figures intersects several conflicting events, e.g., the plate boundary in the lower left. Depending on the chosen thresholds for the identification of conflicting dip situations, the intersecting events were detected and characterized. This can be seen best in Figure 6b with the difference of the emergence angles in subfigures c and d.

Although the multitude of (actually only sparsely covered) attribute sections is difficult to visualize, we can easily make full use of them to simulate the final ZO section including the interference of intersecting events. Furthermore, the approximate time migration included in the current implementation handles all contributing events separately. In contrast, the conventional post-stack time migration is not able to resolve such ambiguities as its input only contains the superposition of all contributing events.

We would like to stress that our proposed approach to handle conflicting dip situations significantly differs from the DMO method: instead of summing along an operator to collect all contributions for *all potential* dips, we detect and characterize a *discrete* number of contributing events. Consequently, our approach provides additional wavefield attributes for subsequent applications, whereas DMO corrects the stack result but does not provide any additional information.

CONCLUSIONS

The pragmatic approach of (Müller, 1998) to perform a ZO simulation by means of the CRS stack method can be adapted to also account for the conflicting dip problem. An additional one-parametric search is required to resolve ambiguities introduced by different events contributing to one and the same ZO sample to be simulated.

The consideration of conflicting dips is necessary to obtain a more physical simulation of a ZO section: the simulated interference of intersecting events is closer to the result of an actual ZO measurement.

In addition to the improved simulated ZO section, the extended CRS stack strategy provides three kinematic wavefield attributes for each particular event, even if it intersects one or more other events (or its own bow-tie segments). Subsequent applications of these wavefield attributes (e. g., an inversion of the macro-velocity model, calculation of Fresnel zones etc.) benefit from this fact, because otherwise the wavefield attributes in the gaps between "broken" event segments would have to be interpolated.

Together with an improved strategy to consider stacking velocity constraints, the extended CRS stack strategy is also better suited to detect and characterize primary events formerly obscured by multiples.

The first results obtained with the extended CRS stack strategy demonstrate that the newly introduced features provide a more realistic simulated ZO section as well as a more complete set of wavefield attributes for subsequent applications. We feel that a more adequate selection of the processing parameters, especially concerning the thresholds used to identify conflicting dip situations, will further improve the results.

As final remark we would like to indicate that the new CRS stack release which includes all newly introduced features is available for download on the WIT homepage. We would strongly appreciate any feedback concerning the installation and application of this code.

REFERENCES

Höcht, G., de Bazelaire, E., Majer, P., and Hubral, P., 1999, Seismics and optics: hyperbolae and curvatures: J. Appl. Geoph., **42**, no. 3,4, 261–281.

Mann, J., Jäger, R., Müller, T., Höcht, G., and Hubral, P., 1999, Common-reflection-surface stack - a real data example: J. Appl. Geoph., **42**, no. 3,4, 301–318.

Mann, J., Hubral, P., Traub, B., Gerst, A., and Meyer, H., 2000, Macro-Model Independent Approximative Prestack Time Migration: 62th Mtg. Eur. Assoc. Expl. Geophys., Extended Abstracts.

Müller, T., 1998, Common Reflection Surface Stack versus NMO/STACK and NMO/DMO/STACK: 60th Mtg. Eur. Assoc. Expl. Geophys., Extended Abstracts.

Müller, T., 1999, The common reflection surface stack - seismic imaging without explicit knowledge of the velocity model: Der Andere Verlag, Bad Iburg.

Schleicher, J., Tygel, M., and Hubral, P., 1993, Parabolic and hyperbolic paraxial two-point traveltimes in 3D media: Geophys. Prosp., **41**, no. 4, 495–514.

Tygel, M., Müller, T., Hubral, P., and Schleicher, J., 1997, Eigenwave based multiparameter traveltime expansions: 67th Annual Internat. Mtg., Soc. Expl. Geophys., Expanded Abstracts, 1770–1773.